Deep-investigated Analytical Modeling of a Surface Permanent Magnet Vernier Motor

Jingwei Zhu, Yuefei Zuo, *Member, IEEE*, Hao Chen, *Member, IEEE*, Jiahao Chen, *Member, IEEE*, and Christopher H. T. Lee, *Senior Member, IEEE*

***Abstract*—Permanent magnet vernier motors (PMVMs) possess the advantage of high torque density for high performance applications. However, the low power factor challenge makes it unacceptable for direct-drive applications. A lack of accurate model based on the motor sizing law raises difficulties for machine designers to further conduct research on the performance metrics. This paper presents a deep investigation into the analytical modeling technique for surface permanent magnet vernier motors (SPMVMs) to identify an accurate approach to obtain the performance metrics, including electromagnetic torque and power factor. The modeling technique is developed based on the conformal mapping method, by using which both radial and tangential permeability functions are calculated to obtain the motor magnetic loading accurately considering the leakage flux. Then, the slotting effect on both air gap flux density and armature winding function is analyzed to achieve a precise formula for torque and power factor computation. The new modeling technique is applied to integral-slot SPMVMs with different slot/pole combinations, gear ratios, slot openings and magnet thickness to evaluate the influence of motor parameters on high power factor and torque density design. Finally, an SPMVM with the characteristics of high torque density and power factor is fabricated to verify the analytical model at the power rating of 0.8 kw and the speed of 500 r/min. The experimental results shows that the prototype exhibits a high power factor of 0.9 and high torque density 22.5 Nm/L.**

***Index Terms*—Permanent magnet, vernier motor, analytical modeling, finite element analysis**

I. Introduction

FOR low-speed applications, such as electric vehicles (EVs) and wind turbines, a high-speed motor with a reduction gearbox is an attractive solution to achieve a high-power-density and high-efficiency system [1]. However, combining an electric motor with the reduction gears, typically multistage or compound planetary ones, results in several issues associated with the drive system. These include the bulky volume and heavy weight of the gear system, gearbox maintenance and additional transmission loss in the gearbox. It is estimated that for a two-stage gearbox, the efficiency at partial load can be as low as 70% [2], which significantly decreases the efficiency of the drive system.

Flux modulation motors integrate the functionality of a gearbox and a high-speed electric motor into a single low-speed and high-torque electric machine to potentially overcome the disadvantages of the gear system by utilizing magnetic gearing effect. One of the candidates that is gaining interest for use in low-speed direct-drive system is the permanent magnet vernier motor (PMVM) due to its simple and compact mechanical structure as well as high-torque-density feature [3]. Historically, development efforts on vernier motors date back to 1963 [4], when Lee constructed the first reluctance version; and the permanent magnet (PM) version emerged in 1995 [5]. There has been significant recent interest in investigating the torque characteristics of PMVMs. In [6], the authors investigate a hybrid excitation PMVM with both acceptable torque density and bi-directional flux regulation by using DC field excitation. Li *et al.* [7] identify the optimal flux modulation pole number to achieve maximum output torque for the PMVM with divided teeth design. It is also shown in [8] that the stator slot PMs and field winding are utilized to improve the torque density by coupling with the redundant harmonics in the air gap. In [9], Xu presents the idea of hybrid stator fault-tolerant PMVMs; the comparison with conventional PM motors is made to demonstrate the torque performance improvement of the proposed design.

While PMVMs exhibit the potential for high-torque-density applications, the low power factor issue remains a key challenge. Recently, several new topologies have been presented to improve the power factor. In [10], a surface-mounted PMVM (SPMVM) with two-slot-pitch concentrated winding is designed to reduce the harmonic components and phase inductance, thus increasing the power factor. However, this design increases the complexity of the winding layout and the torque density is less than 16 Nm/L. A prototype of a double-stator spoke array PMVM [11], is constructed to achieve high power factor by providing a flux bridge between two stators, and high torque density by increasing the surface area and flux density in the air gap. However, the issues of complicated mechanical structure and reliability still need to be fixed based on specific applications. Even though new motor configurations emerge, there lacks insufficient deep research on the accurate analytical modeling of the PMVM to explain the relationship between motor performance metrics. In [12]–[14], the motor performance metrics, including air gap permeability, flux density and torque, are calculated according to the analytical model. However, the air gap permeability model is based on [15] which is applied to permanent magnet brushless DC motors with small slot openings, while for PMVMs with large slot openings ratios, typically between 0.3 - 0.5, the accuracy may be reduced; moreover, the slotting effect on armature winding side is not considered. An investigation of scaling effect of the PMVM has been conducted by Padinharu *et al.* in [16], [17] based on an improved analytical model; however, the reason

why exponential function is assumed to represent the air gap permeability values at different angle positions is unclear, and the effect of stator tooth width and permanent magnet thickness on the leakage flux evaluation is neglected. Hence, there still exisits challenges and opportunities in developing an accurate analytical model for PMVMs.

The main contribution of this paper is to propose a comprehensive and accurate analytical model for integral-slot winding SPMVMs considering the leakage flux and slotting effect. The improved model is proved to be suitable for motors with different slot/pole combinations and gear ratios. Firstly, the magnetic loading modeling, including the main and modulated flux densities computation, is implemented; the investigation is conducted on the basis of the air gap permeability function in both radial and tangential directions. Secondly, the flux linkage modeling technique is introduced to separate the contribution of various harmonic components; this technique extends the modeling efforts by considering the influence of slotting effect on winding factor, which is quite essential, but lacks sufficient discussion in previous research on PMVM design. Next, motor performance metrics, including torque and power factor, are evaluated based on the modeling technique; and the effect of geometric parameters on high power factor and torque density design is discussed. Finally, an SPMVM with the feature of high power factor and torque density is manufactured. The experimental results confirm the validity of the analytical model used in the paper.

II. Magnetic Loading Modeling

This section derives a magnetic loading model for PMVMs. In electric machine sizing, the performance metrics are related to the fundamental properties: electric loading and magnetic loading. However, PMVMs possess a variety of magnetic working harmonics and significant leakage flux, both of which raise difficulties for an accurate model for magnetic loading. It should be noted that an analytical model has been proposed in [12] and the slot opening effect is derived by a cosine function with the coefficient calculated by conformal mapping method; however, for large slot openings, the cosine function may not be accurate enough for the actual air gap permeance. In another prior work [16], the exponential function is selected for an improved air gap permeance function. However, there lacks sufficient explanation on how to derive the function and the reason why exponential form is selected to represent the permeance function is not clear; moreover, only the radial permeance is taken into consideration and the effects of both slot opening and magnet thickness are neglected in leakage flux calculation, which may affect the accuracy of the modeling.

The modeling technique in this section extends analysis of the conformal transformation in [15], where only the minimum value of the radial air gap permeability is calculated by the conformal mapping method, to evaluate the permeability value over the circular air gap in both radial and tangential direction. The radial component is mainly utilized to compute the effective flux density while the tangential one contributes to leakage flux calculation. The magnetic loading model has been applied to integral-slot winding PMVMs with 12-slot 20-pole,

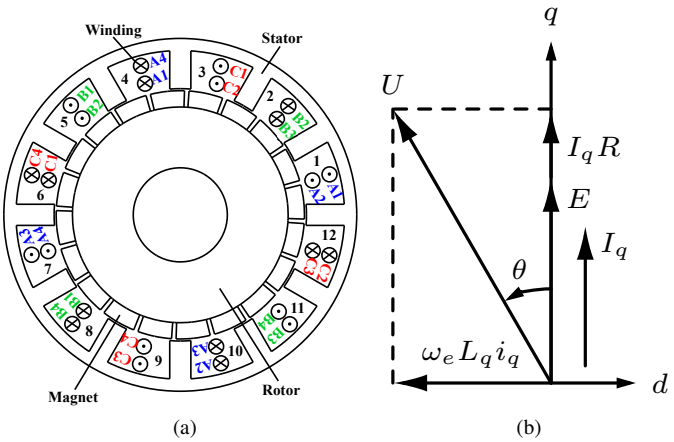

Fig. 1. PMVM (a) Geometry of 12/20 topology (b) Phasor vector (I_d=0)

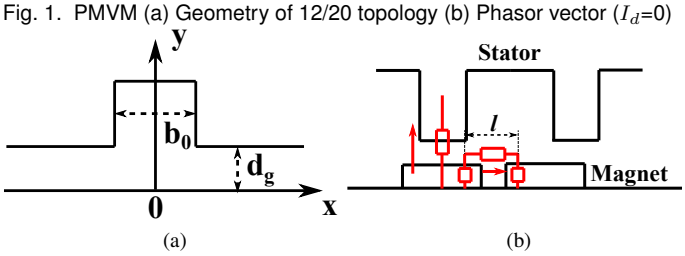

Fig. 2. Schematics (a) z plane conformal mapping (b) Flux path

12-slot 22-pole, 24-slot 44-pole, 18-slot 34-pole and 24-slot 46-pole combinations, which satisfies the principle of P_r=S-P_s to confirm its validity for various slot openings, magnet thickness, slot/pole and gear ratio (G_r) combinations. Here, P_r is the rotor pole pair number, P_s the armature winding pole pair number and S the slot number. The schematic of motor configuration (12/20) is shown in Fig. 1a.

A. Air Gap Permeability Modeling

Conformal mapping method is used for a bounded region in the form of a complex vector. For magnetic flux distribution, where slot effect exists, it is quite suitable to utilize conformal mapping to transform the boundary shape into the complex plane and calculate the air gap permeability. The procedure is similar to that implemented in [15], including mapping to z plane, using Schwarz-Christoffel transformation from z to w plane and finally z to t plane representing slotless structure. The mapping in z plane is shown in Fig. 2a, in which one slot model is utilized. The relationship between z and w is given as follows

$$z = \frac{b_0}{\pi}\left[\arcsin\frac{w}{a} + \frac{d_g}{b_0}\ln\left(\frac{\sqrt{a^2-w^2}+\frac{2d_g}{b_0}w}{\sqrt{a^2-w^2}-\frac{2d_g}{b_0}w}\right)\right] \quad (1)$$

where d_g is the equivalent magnetic air gap length and a is derived as

$$a = \sqrt{1+\left(\frac{2d_g}{b_0}\right)^2} \qquad d_g = g + h_m/\mu_m \quad (2)$$

here, g is the actual air gap length, h_m is the magnet thickness and μ_m is relative permeability of the magnet. By using w to t transformation, the relative permeability λ with the scaled value μ_0/d_g can be determined

$$\lambda = \frac{1}{\sqrt{1+\left(\frac{b_0}{2d_g}\right)^2-\left(\frac{b_0}{2d_g}w\right)^2}} \quad (3)$$

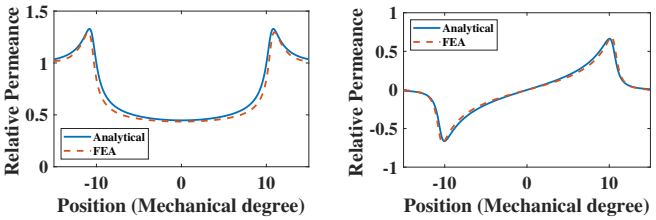

Fig. 3. Analytical & FEA of air gap permeability (a) radial (b) tangential

Then, back to the z plane, the position over the circular air gap can be expressed as a complex vector

$$z = c + \left(\frac{h_m}{\mu_m} + m \cdot g\right) j \qquad c \in \left(-\frac{\tau_s}{2}, \frac{\tau_s}{2}\right),\ m \in (0,1) \tag{4}$$

here, τ_s is the slot pitch while m is the coefficient representing the position in radial direction from the surface of the magnet to that of the stator tooth. w can be calculated by solving Eq.(1) at a fixed position z in the air gap. Then, by substituting w into Eq.(3), λ is obtained with the real part and image part as the permeability value in the radial and tangential direction, respectively. By selecting the stator tooth arc ratio β as 0.3, air gap length g as 0.6 mm and magnet thickness as 5 mm for a 12-slot stator, the air gap permeability waveforms over one slot pitch in both radial and tangential directions using the conformal transformation are shown in Fig. 3a-3b, respectively, while compared with the FEA results. The results indicate that the analytical model by using conformal mapping is well complied with FEA. Thereby, λ can be derived in the complex form

$$\lambda = \lambda_r + \lambda_\theta j \tag{5}$$

According to the mapping results in z plane (see Fig.2a), the slotless air gap flux density can be modeled as

$$B = B_\theta + B_r j \tag{6}$$

where the fundamental radial component B_r and tangential component B_θ are calculated by the method in [18]

$$B_r = \frac{4B_{rr}}{\pi\mu_r}\sin\left(\frac{\pi\alpha}{2}\right)\frac{P_r}{{P_r}^2-1}\left[\left(\frac{r}{R_s}\right)^{P_r-1}\left(\frac{R_m}{R_s}\right)^{P_r+1}+\left(\frac{R_m}{r}\right)^{P_r+1}\right]\cos\left(P_r\theta_s-\omega_e t\right)\left\{\frac{P_r-1+2\left(\frac{R_r}{R_m}\right)^{P_r+1}-(P_r+1)\left(\frac{R_r}{R_m}\right)^{2P_r}}{\frac{\mu_r+1}{\mu_r}\left[1-\left(\frac{R_r}{R_s}\right)^{2P_r}\right]-\frac{\mu_r-1}{\mu_r}\left[\left(\frac{R_m}{R_s}\right)^{2P_r}-\left(\frac{R_r}{R_m}\right)^{2P_r}\right]}\right\} \tag{7}$$

$$B_\theta = \frac{4B_{rr}}{\pi\mu_r}\sin\left(\frac{\pi\alpha}{2}\right)\frac{P_r}{{P_r}^2-1}\left[-\left(\frac{r}{R_s}\right)^{P_r-1}\left(\frac{R_m}{R_s}\right)^{P_r+1}+\left(\frac{R_m}{r}\right)^{P_r+1}\right]\sin\left(P_r\theta_s-\omega_e t\right)\left\{\frac{P_r-1+2\left(\frac{R_r}{R_m}\right)^{P_r+1}-(P_r+1)\left(\frac{R_r}{R_m}\right)^{2P_r}}{\frac{\mu_r+1}{\mu_r}\left[1-\left(\frac{R_r}{R_s}\right)^{2P_r}\right]-\frac{\mu_r-1}{\mu_r}\left[\left(\frac{R_m}{R_s}\right)^{2P_r}-\left(\frac{R_r}{R_m}\right)^{2P_r}\right]}\right\} \tag{8}$$

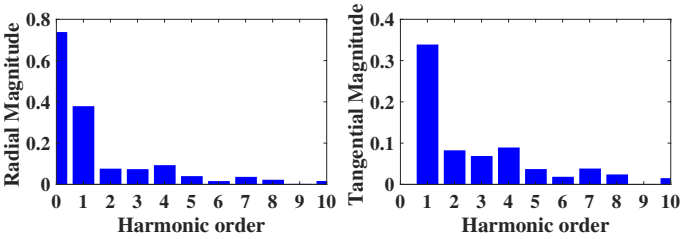

Fig. 4. DFT of the air gap permeability function (a) radial (b) tangential

Here, B_{rr} is the remanence of the magnet, α is the magnet pole arc ratio (θ_m/θ_p, see Fig. 10b), P_r is the rotor pole number, r is the air gap radius, R_s is the stator inner radius, R_m is the rotor outer radius, R_r is the rotor core radius and θ_s is the rotor position angle. As a result, the flux density B_s in the slotted air gap is expressed as

$$\begin{aligned} B_s = B \cdot \lambda &= (B_\theta\lambda_r - B_r\lambda_\theta) + (B_r\lambda_r + B_\theta\lambda_\theta)\, j \\ &\approx -B_r\lambda_\theta + B_r\lambda_r j \end{aligned} \tag{9}$$

where, the imaginary part represents the flux density in the radial direction while the real one is that in the tangential direction according to the layout in Fig.2a. It can be seen that the dominant B_r (neglecting B_θ due to small value) contributes to the tangential component in the slotted air gap, which is beneficial to leakage flux computation in the next subsection.

B. Magnet Leakage Flux Modeling

Due to severe leakage flux and complicated flux path, the approach of magnetic equivalent circuit (MEC) may encounter difficulty for accurate modeling; furthermore, MEC may change with the rotor position and motor geometry parameters, including stator tooth arc ratio and rotor pole number. Thereby, in this subsection, a leakage flux evaluation method of utilizing the tangential air gap permeance is presented since Eq. (9) has indicated the possibility of achieving this.

A schematic of the flux path is illustrated in Fig. 2b, which is composed with two kinds of flux lines: one passing the stator teeth as the main flux, the other going through the magnets and the tangential air gap as the leakage flux. The length of the tangential air gap l is estimated as

$$l = \tau_r\left(1 - \alpha/2\right) \tag{10}$$

here, τ_r is the rotor pole pitch. For SPMVMs, since τ_r is smaller than τ_s, one-slot model of conformal transformation is still valid. Meanwhile, due to the existence of magnet leakage flux over the whole air gap circle (mechanical angle 360°), the tangential air gap permeability function within a slot pitch distance can be used to calculate the average permeability in tangential direction.The tooth tip and adjacent magnet pole leakage flux are two main sources, both of which have been considered in the tangential air gap permeability function with slotting effect.

The DFT of the analytical permeability data in Fig. 3 is displayed in Fig. 4a-4b, respectively in both radial and tangential directions. Therefore, the air gap permeability functions λ_r

(radial) and λ_θ (tangential) are given as follows

$$\begin{aligned}\lambda_r &= \lambda_0 + \sum_{k=1} \lambda_k \cos\left(kS\theta_s\right) \\ \lambda_\theta &= \sum_{k=1} \lambda^{'}{}_k \sin\left(kS\theta_s\right)\end{aligned} \tag{11}$$

It can be seen from Fig. 4a that the first two terms are the dominant components (others neglected) and the air gap flux density neglecting the leakage flux is calculated as

$$\begin{aligned}B_g\left(\theta_s, t\right) &= B_r \lambda_r \\ &\approx B_{(P_r)} \cos\left(P_r\theta_s - \omega_e t\right) + B'_{(P_s)} \cos\left(P_s\theta_s + \omega_e t\right) \\ &\quad + B_{(S+P_r)} \cos\left((P_r + S)\theta_s - \omega_e t\right) \\ B_{(P_r)} &= B_1\lambda_0,\ B'_{(P_s)} = B_{(S+P_r)} = B_1\frac{\lambda_1}{2}\end{aligned} \tag{12}$$

where, B_1 the fundamental amplitude of slotless flux density. It is confirmed that flux densities with P_r and P_s pole pair numbers contribute most to the output torque [3], [12], and thereby, they are investigated for accurate modeling, especially the modulated component $B'_{(P_s)}$ due to a lack of sufficient research on it. It can be deduced from Fig. 4b and Eq.(9) that the leakage flux, which is in the tangential direction, mainly comes from $B'_{(P_s)}$ because almost zero DC component and large first order amplitude in the tangential air gap permeability lead to much more significant leakage for $B'_{(P_s)}$ than $B_{(P_r)}$. Hence, the leakage flux computation will focus on that from $B'_{(P_s)}$ while neglecting that from $B_{(P_r)}$ due to the small amount. In addition to the tangential air gap permeability, magnet reluctance also needs to be considered to form a flux circle (see Fig. 2b) for leakage flux computation. Since the value of $\lambda^{'}_1$ is scaled by the length of d_g, the updated relative permeability $\lambda^{''}_1$ regarding the actual length l is specified as

$$\lambda^{''}{}_1 = \lambda^{'}{}_1 \cdot d_g/l \tag{13}$$

Similarly, the relative magnetic reluctance of the magnet is obtained as

$$R = h_m/(\mu_r d_g) \tag{14}$$

Hence, the effective flux density $B_{(P_s)}$ can be determined by two flux paths (main and leakage) demonstrated in Fig. 2b

$$B_{(P_s)} = B'_{(P_s)} \frac{\frac{\lambda_1}{\lambda^{''}{}_1} + 2\lambda_1 R}{\frac{\lambda_1}{\lambda^{''}{}_1} + 2\lambda_1 R + 1} \tag{15}$$

C. Comparative Accuracy Analysis

The above analytical method for $B_{(P_s)}$ is applied to SPMVMs with different values of stator tooth arc ratio β (β=θ_t/θ_{slot}), magnet thickness h_m, slot/pole combinations and G_r under the condition of 100°C. The results are compared with those from FEA and the conventional analytical method not considering the leakage flux. Fig. 5 shows the flux density values and analytical errors compared with FEA (modulated one named "Modu" in the legend) of the 12/20 SPMVM with β ranging from 0.3 - 0.5 and h_m from 2 mm - 6 mm while Fig. 6 presents the analytical errors of 12/22, 24/46, 18/34 and 24/46 topologies with the same β at 0.5 and h_m from 2 mm - 6 mm. Other motors' geometry parameters are summarized in Table I, where D_{os} is the stator outer diameter and D_{or} the rotor outer diameter as depicted in Fig. 10b, l_e is the stack length. Fig. 5a (left y axis for the main flux density and right y axis for the modulated one) demonstrates that analytical results of the modulated flux density is well consistent with that of FEA under a variety of conditions while analytical method without leakage correction may exhibit huge discrepancy (more than 60% for 12/20 and over 150% for 24/46). This difference may affect torque calculation to a great extent due to the component of G_r multiplying $B_{(P_s)}$ [3], which will be discussed in detail in Section IV. In the main flux density comparison, the difference is within 10% and will not lead much difference for motor performance analysis. It is evident from Fig. 5-6 that the discrepancy of the conventional method is observed to increase with the magnet thickness, which can be explained by the increasing leakage flux caused by the permeability change. Fig. 7a (12/20 PMVM with β = 0.3) indicates that the tangential relative permeability is increasing with a constant rate while the radial one gradually reduces at a smooth rate. The ratio of radial air gap permeability to leakage flux path permeability, defined as v, can be obtained from Fig. 7b. It is evident that the leakage component boosts significantly with regard to the magnet thickness increase, which, in turn, results in an extensively decrease in the modulated flux density i.e. $B_{(P_s)}$. Fig. 8a (12/20 PMVM with h_m = 4 mm) presents the permeability results with various stator tooth arc ratio β; and both radial and tangential components of modulated flux density increases to peak point at around β = 0.3 and then keeps decreasing simultaneously, resulting in a significant reduction of modulating effect. However, there exists no apparent variation of v (see Fig. 8b), indicating the insensitivity of leakage flux percentage to the slot opening.

Based on the analysis from this section, one concludes that leakage flux acts as an important role in flux density modeling of SPMVMs, especially for the modulated one; magnet thickness h_m exhibits a significant effect on the leakage flux percentage.

TABLE I
MAIN GEOMETRY PARAMETERS

Motor topology	12/20	12/22	24/44	18/34	24/46
P_s	2	1	2	1	1
P_r	10	11	22	17	23
G_r	5	11	11	17	23
D_{os} (mm)			120		
g (mm)			0.6		
l_e (mm)			70.2		
α			0.9		
D_{or} (mm)	84.61	79.01	86.65	84.30	83.50

III. FLUX LINKAGE MODELING

The flux linkage calculation, as depicted in Eq. (16), depends mainly on accurate modeling of magnetic flux density, which is developed in Section II, and the winding function.

$$\varphi_f = l_e \frac{D_{is}}{2} \int_0^{2\pi} N\left(\theta_s\right) B_g\left(\theta_s, t\right) \mathrm{d}\theta_s \tag{16}$$

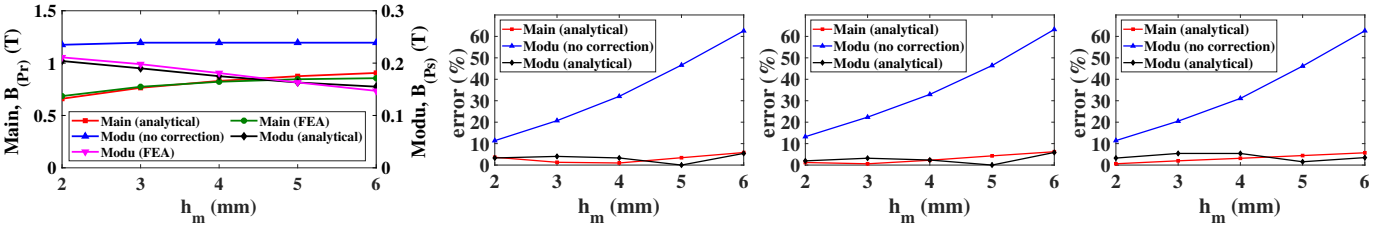

Fig. 5. Main & modulated components for 12/20 SPMVM. (a) Flux density with β = 0.3. Analytical error: (b) β = 0.3 (c) β = 0.4, (d) β = 0.5

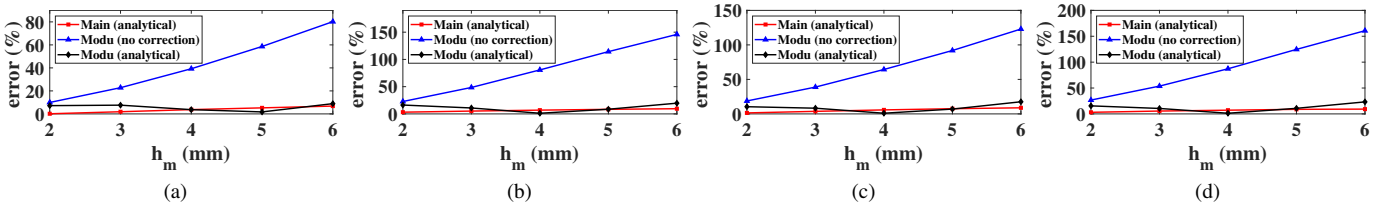

Fig. 6. Main & modulated analytical error (a) 12/22 (G_r=11) (b) 24/44 (G_r=11) (c) 18/34 (G_r=17) (d) 24/46 (G_r=23) SPMVMs with β = 0.5

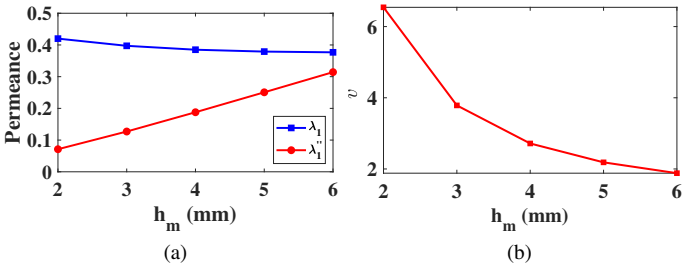

Fig. 7. Permeability post-processing for β = 0.3 (a) trend of λ_1 & $\lambda_1^{''}$ VS magnet thickness (b) permeability ratio in radial direction to that of total leakage path

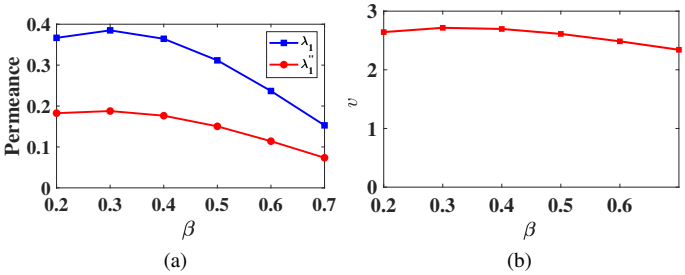

Fig. 8. Permeability post-processing for h_m = 4 mm (a) trend of λ_1 & $\lambda_1^{''}$ VS stator tooth arc ratio (b) permeability ratio in radial direction to that of total leakage path

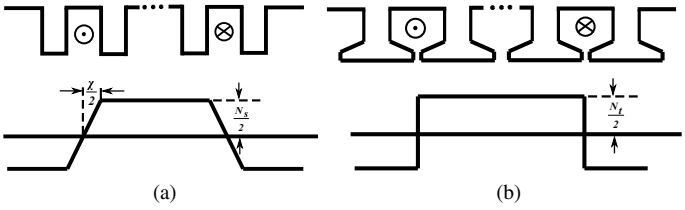

Fig. 9. Winding function (a) slotting (b) non slotting

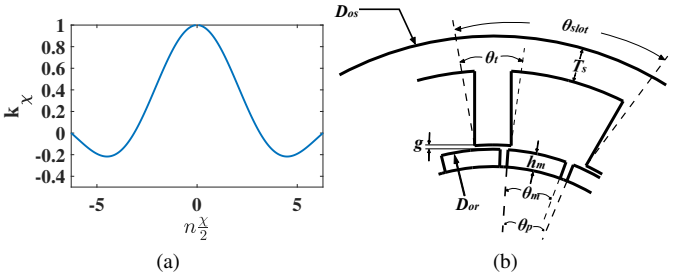

Fig. 10. (a) k_χ VS $n\frac{\chi}{2}$ (b) geometry parameters for the SPMVM

However, insufficient investigation has been presented for slot opening effect on winding function in magnetic geared machines. The slotting effect on the winding function is discussed by Lipo for induction machines [19]. Due to the semi-closed slot structure of induction machines and the feature of only fundamental component utilized, the slotting effect can be neglected. However, this effect will have a significant impact on PMVMs since the slot opening ratio is usually more than 0.5 and high order harmonics are used to generate flux linkage.

1) *Slot Opening Factor Analysis*: The schematics of the winding function with and without slotting effect are shown in Fig. 9a - 9b, where χ is the slot opening angle in electrical degree and N_s is the turn number per phase in series. The winding function of the slotted structure can be calculated as

$$N(\theta_s) = \frac{4}{\pi}\left[\int_0^{\frac{\chi}{2}} \frac{N_s}{\chi}\theta\sin(n\theta)\,\mathrm{d}\theta + \int_{\frac{\chi}{2}}^{\frac{\pi}{2}} \frac{N_s}{2}\sin(n\theta)\,\mathrm{d}\theta\right] = \frac{2}{\pi}\frac{N_s}{n}\frac{\sin\left(n\frac{\chi}{2}\right)}{n\frac{\chi}{2}} \tag{17}$$

here, n is the harmonic order. Since for square waveform as shown in Fig. 9b, the amplitude is $\frac{2N_s}{\pi n}$, the slotting effect contributed to $N(\theta_s)$ is a factor of k_χ.

$$k_\chi = \sin\left(n\frac{\chi}{2}\right)/n\frac{\chi}{2} \tag{18}$$

The relationship between k_χ and $n\frac{\chi}{2}$ can be obtained in Fig. 10a between -2π and 2π. It can be extracted that when X-axis is close to 0, the value of Y-axis is almost equal to 1 with quite small reduction; whereas, the declining speed is increasing significantly while the coordinate of X-axis is away from zero point; moreover, there is possibility for k_χ to reach the value below zero (between π and 2π). For PMVMs, due to the characteristics of large slot opening (large χ) and high order harmonics (large n) utilized, the slot opening will have a significant effect on the reduction of winding function, thus

declining the effective flux linkage. Eq. (18) can be specified for the harmonic with P_r pole pair number of PMVMs as

$$k_\chi = \frac{\sin\left[G_r \cdot P_s \cdot \frac{2\pi}{S}(1-\beta)\right]}{G_r \cdot P_s \cdot \frac{2\pi}{S}(1-\beta)} = \frac{\sin\left(\frac{P_r}{S}(1-\beta)\pi\right)}{\frac{P_r}{S}(1-\beta)\pi} \tag{19}$$

Similar computation process can be applied to harmonic with $P_r + S$ pole pair number. Thereby, eq. (16) can be further developed as

$$\varphi_f = D_{is} l_e N_s k_{d1} k_{p1} \left(\frac{k_{P_r} B_{(P_r)}}{P_r} + \frac{k_{P_s} B_{(P_s)}}{P_s} + \frac{k_{(S+P_r)} B_{(S+P_r)}}{S+P_r}\right) \tag{20}$$

where k_{P_s}, k_{P_r} and $k_{(P_s+S)}$ represent the slot opening factors associated with $B_{(P_s)}$, $B_{(P_r)}$ and $B_{(P_s+S)}$, respectively; k_{d1} and k_{p1} is the distribution and pitch factor (k_{p1}=1 for full pitch) of the fundamental component, respectively. The slot opening factor k_χ of the above three working harmonics for PMVMs with various slot openings and slot/pole combinations are displayed in Table II. It is obvious that PMVMs with $P_r = S - P_s$ possess a gradually decreasing slot opening factor for $B_{(P_r)}$ against the increasing G_r with the same slot opening while candidates with the same G_r (see the gray highlighted column) exhibits identical slot opening factors regardless of slot/pole combinations. Even though the slot opening may be extremely large for PMVMs, the fundamental component is still able to show a quite high slot opening factor (usually > 0.975), while the slot harmonic displays its feature of significantly reduced one (< 0.5). It can be also seen that, with the same slot and winding configuration, the rotor pole pair selection of $P_r = S - P_s$ exhibits a much larger k_{P_r} than that of $P_r = S + P_s$ (see the red and blue colored fonts), which contributes to more effective flux linkage and explains the reason why the choice of $P_r = S - P_s$ is able to achieve better performance for PMVMs in consistence with the initial discussion in [3]. Moreover, considering the value of $k_{(P_r+S)}$ and Eq. (20), the contribution of $B_{(S+P_s)}$ to the flux linkage can be neglected ($< 2\%$).

2) *Comparison Based Accuracy Analysis*: 12/20 (G_r=5) and 12/22 (G_r=11) PMVMs, with h_m = 4 mm and other geometry listed in Table I, are selected to confirm the validity of slot opening factor analysis. The flux linkage versus various value of β can be found in Fig. 11a - Fig. 11b, respectively, with "1" representing the totally analytical results, "2" flux density B_g using FEA while winding function N utilizing analytical modeling, "3" FEA results and "4" flux density B_g using FEA while winding function N using conventional method neglecting the slot opening effect. It is evident that curve "2" matches quite well with "3" (error $< 3\%$), indicating the accuracy of the winding function modeling, while the discrepancy can reach approximate 40% without slot opening consideration. The small difference between curve "1" and "3" ($< 6\%$) demonstrates the preciseness of the entire modeling technique. It can also be extracted that the peak values of φ_f with different G_r possess their own unique β, i.e. 0.5 for 12/20 and 0.4 for 12/22 topology. However, as for torque or power factor analysis, flux linkage is just one of the essential factors while electric loading also needs to be considered critically,

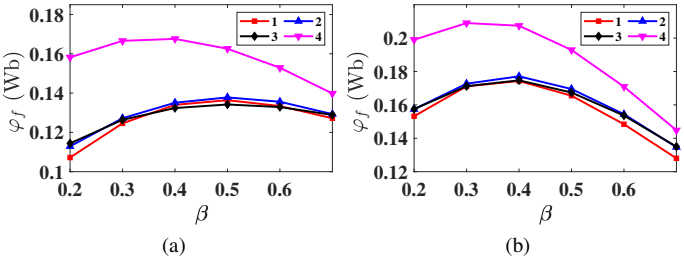

Fig. 11. Flux linkage evaluation (1: totally analytical results, 2: B_g using FEA while N utilizing analytical modeling, 3: FEA results, 4: B_g using FEA while N using conventional method) for (a) 12/20 (b) 12/22 SPMVMs with h_m = 4 mm

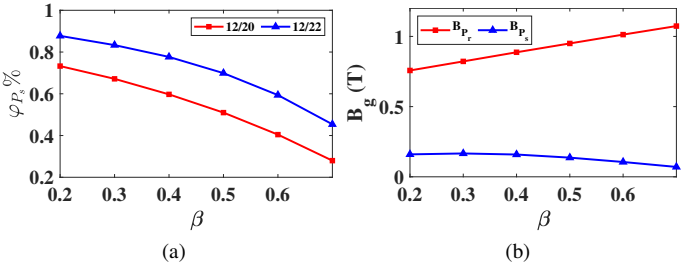

Fig. 12. (a) Ratio of φ_{P_s} (b) 12/20 flux density versus β

which is discussed in detail in Section IV. The proportion of the flux linkage generated by $B_{(P_s)}$ is demonstrated in Fig. 12a. It can be observed that the ratio of the modulated component drops against the slot opening, which can be explained by the variation law of the flux density (see Fig. 12b), while SPMVMs with larger G_r possess a higher percentage of φ_{P_s} over the β range. It is obvious from Eq. (20) and Table II that large G_r (P_r/P_s) compensates for the gap of reduced k_{P_r} and increases the proportion of the modulated flux linkage.

The slot opening analysis proposed in this section is intended to enable the motor designers to consider the slotting effect on the winding function which significantly influences the performance of vernier machines. Meanwhile, the contribution of the each working harmonics is calculated and analyzed.

IV. Motor Metrics Analysis

This section provides an analytical model of torque and power factor for SPMVMs on the basis of the method proposed in Section II and III. 12/20 topology is selected to investigate the proposed modeling technique due to its capability of achieving high torque density and power factor simultaneously. It extends the analysis based on electric loading and magnetic loading to determine the relationship between torque and power factor.

A. Power Factor Calculation

According to the phasor diagram illustrated in Fig. 1b, where, E is the no-load back EMF and U is the terminal voltage the power factor is determined

$$PF = \cos\theta = \frac{1}{\sqrt{1 + \left(\frac{\omega_e L_q i_q}{i_q R + \omega_e \varphi_f}\right)^2}} \tag{21}$$

where L_q and i_q are the inductance and current in q axis; ω_e is the electrical angular frequency. Neglecting the winding resistance R, (21) can be further simplified as [20]

$$PF = \frac{1}{\sqrt{1 + \left(\frac{L_q i_q}{\varphi_f}\right)^2}} = \frac{1}{\sqrt{1 + K^2}} \tag{22}$$

TABLE II
LIST OF k_χ FOR PMVMS WITH DIFFERENT SLOT OPENINGS & SLOT/POLE COMBINATIONS

P_r classification	S	P_s	P_r	G_r	$\beta = 0.3$			$\beta = 0.5$			$\beta = 0.7$			q	k_{d1}
					k_{P_s}	k_{P_r}	$k_{(P_r+S)}$	k_{P_s}	k_{P_r}	$k_{(P_r+S)}$	k_{P_s}	k_{P_r}	$k_{(P_r+S)}$		
$P_r = S + P_s$	12	2	14	7	0.978	0.212	-0.21	0.989	0.527	-0.076	0.996	0.81	0.436	1	1
	12	1	13	13	0.994	0.289	-0.216	0.997	0.583	-0.04	0.999	0.835	0.471	2	0.966
$P_r = S - P_s$	12	2	10	5	0.978	0.527	-0.193	0.989	0.738	0.09	0.996	0.9	0.572	1	1
	12	1	11	11	0.994	0.448	-0.209	0.997	0.689	0.043	0.999	0.88	0.538	2	0.966
	24	2	22	11	0.994	0.448	-0.209	0.997	0.689	0.043	0.999	0.88	0.538	2	0.966
	18	1	17	17	0.998	0.421	-0.212	0.999	0.672	0.029	0.9995	0.873	0.527	3	0.960
	24	1	23	23	0.999	0.408	-0.213	0.999	0.663	0.021	0.9997	0.87	0.522	4	0.958

Neglecting the leakage inductance and considering slotting effect on the inductance [21], where the coefficient γ is introduced, L_q is specified using magnetic equivalent circuit [19] as follows

$$L_q = \frac{3}{2}\frac{8}{\pi}\left(\frac{k_1 N_s}{2P_s}\right)^2 \mu_0 \frac{D_{is} l_e}{d_g}(1 - 0.8\gamma) \tag{23}$$

here, k_1 is the winding factor of the fundamental component (neglecting the slotting effect) and γ is defined as half the difference between the relative radial permeability value at -15° and 0° (see Fig. 3a). Substituting Eq. (20) and (23) into (22), K is calculated as

$$\begin{aligned} K &= \frac{\mu_0 D_{is} A\,(1 - 0.8\gamma)}{2P_s d_g\left[\frac{k_{P_r} B_{(P_r)}}{G_r} + k_{P_s} B_{(P_s)}\right]} \\ A &= \frac{6 k_1 N_s I_q}{\pi D_{is}} \end{aligned} \tag{24}$$

where A is the linear current density (electric loading). It can be seen from (22) that smaller K will lead to higher power factor and therefore a PMVM with low electric loading and high combined magnetic loading implies a high power factor.

B. Torque Calculation

For electric machine sizing, the torque performance is in proportional to the electric loading, magnetic loading and rotor volume. For SPMVM sizing, the torque equation can be derived from synchronous motor [19].

$$\begin{aligned} T_e &= \frac{3}{2} P_r \varphi_f I_q \\ &= \frac{\pi}{4} {D_{is}}^2 l_e G_r \left(\frac{k_{P_r}}{G_r} B_{(P_r)} + k_{P_s} B_{(P_s)}\right) A \end{aligned} \tag{25}$$

Therefore, the magnetic loading B for PMVMs is $k_{P_r} B_{(P_r)} + G_r k_{P_s} B_{(P_s)}$ and the expression $\frac{k_{P_r}}{G_r} B_{(P_r)} + k_{P_s} B_{(P_s)}$ in (24) is defined as "sub-magnetic loading" B_{sub} in this paper.

$$B = G_r B_{sub} \tag{26}$$

Since B_{sub} has a small value due to small amplitude of modulated flux density $B_{(P_s)}$, a high gear ratio dividing the largest flux density component $B_{(P_r)}(B_{(P_r)}/G_r)$ and significantly reduced slot opening factor k_{P_r}, low power factor issue of PMVMs appears. Therefore, to achieve a high torque density and high power factor PMVM, an effective solution need to be considered with the following aspects: reasonable electric loading, large magnetic loading, suitable gear ratio and stator pole pair number.

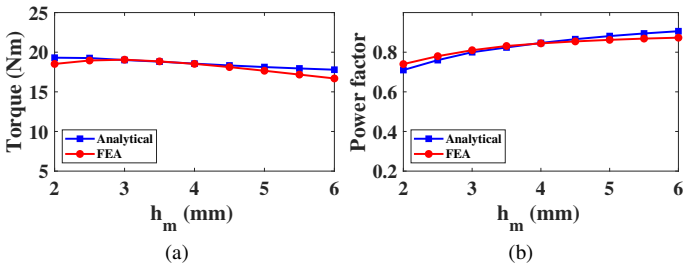

Fig. 13. Analytical & FEA comparison of performance metrics versus h_m (a) Torque (b) Power factor

C. Accuracy Analysis & Comparison

It is obvious from Eq. (24) and (22) that topologies with P_s = 2 possesses better power factor than those with P_s = 1. Meanwhile, the value P_r affects the leakage flux, thus resulting in the variation of B and B_{sub}. Thereby, 12/20 topology is selected for analysis in this section due to the fact that P_s = 2 contributes to a higher power factor and P_r = 10 restricts the component of leakage flux, leading to a suitable value of B and B_{sub}. The geometry and winding configuration of the 12/20 SPMVM are shown in Fig. 1a. The motors' geometry parameters are summarized in Table I with variable h_m and β. The RMS value of current density J is fixed at 5 A/mm^2. The torque performance and power factor analysis of the motor are performed by varying h_m and β over a wide range to assess the comparison between motor parameters. The analytical model and FEA results considers h_m changing from 2 mm to 6 mm and β fixed at 0.3 with the torque and power factor comparison are plotted in Fig. 13a and Fig. 13b, respectively. It can be extracted that the output torque decreases slightly with h_m while the power factor expands. It is obvious from the analytical modeling in Section II that the leakage flux of the modulated component boosts against h_m even though the main component increases, resulting in the torque reduction. According to Eq. (24) and (22), the increased magnetic air gap leads to a boost in power factor. The h_m of 5.5 mm is chosen for a high power factor and torque density design. Fig. 14a and 14b show the torque and power factor variation with β, respectively. It reveals that optimal β for maximum torque is between 0.25 – 0.3 while the power factor value keeps increasing due to reduced slot cross sectional area and linear current density. The analytical modeling and FEA results demonstrate good agreement.

V. HARDWARE PROTOTYPE TEST

A 12/20 SPMVM with the feature of high torque density and power factor was constructed to validate the analytical modeling in Section II, III and IV, respectively, with the

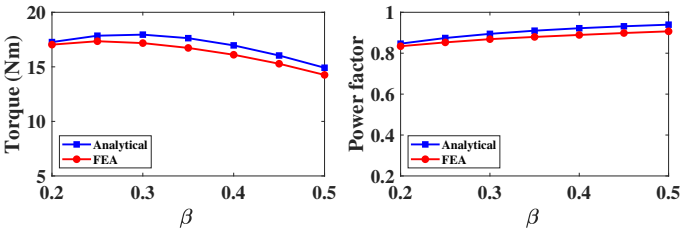

(a) (b)

Fig. 14. Analytical & FEA comparison of performance metrics versus β (a) Torque (b) Power factor

TABLE III
12/20 SPMVM PROTOTYPE PARAMETERS

D_{or} (mm)	h_m (mm)	g (mm)	T_s (mm)	α	β	l_e (mm)
84.43	5.55	0.69	4.14	0.8837	0.3203	70.2

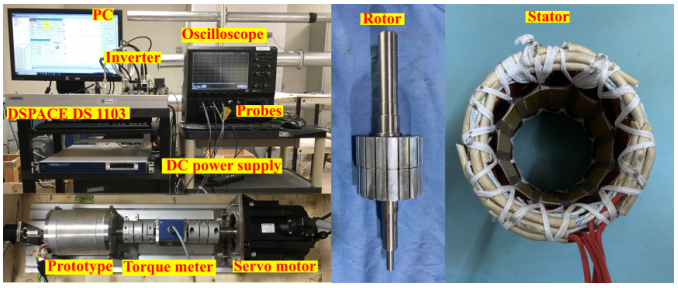

Fig. 15. Photos of the prototype and test bench

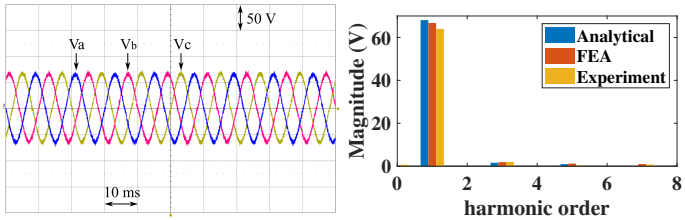

(a) (b)

Fig. 16. No-load back EMF at 500 r/min (a) Experimental waveform (b) FFT result compared with FEA and analytical modeling

machine parameter described in Table III (geometry Fig. 1a), test band shown in Fig. 15. The rated speed is 500 r/min utilizing 135 VDC bus voltage.

First, the no-load test was conducted at the rated speed 500 r/min to validate the back EMF [see Fig. 16]. Note that the comparison results from the experiment, JMAG (20°C) and analytical modeling are clearly in close agreement. Next, the results from measured torque against phase current amplitude are shown in Fig. 17a compared with FEA and analytical approach. The experimental results clearly exhibit good agreement with the simulation model (60°C) over a wide range of current. Fig. 17b depicts the flux density distribution with the current density 5.3 A/mm^2 (10.4 A). It is noticeable that under rated condition, the saturation level of the electrical steel is not high, indicating a good overload capability for this topology. Fig. 18 shows the three-phase current and torque waveforms with the current density 5.3 A/mm^2 and speed of 500 r/min. A comparison of phase current and phase to neutral voltage between the measured and simulated results is shown in Fig. 19, where V_a is the A phase voltage generated by the VSI and V_{af} is that after filtering the high frequency switching harmonics. The measured performance data are presented in Table IV (TMV: torque per unit of active motor volume).

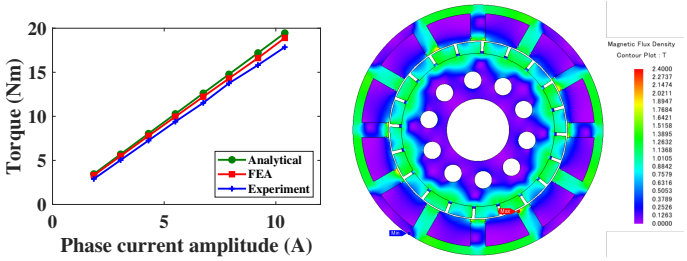

(a) (b)

Fig. 17. Prototype 500 r/min (a) Torque versus current (b) Flux density distribution

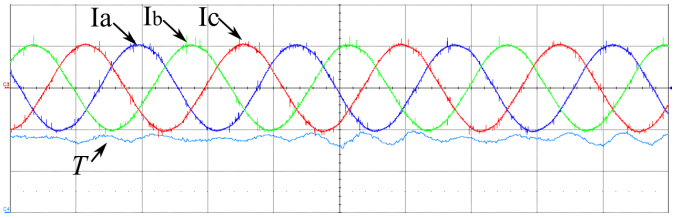

Fig. 18. Measured current and torque waveforms at 500 r/min (5 ms/div, 10 A/div and 10 Nm/div)

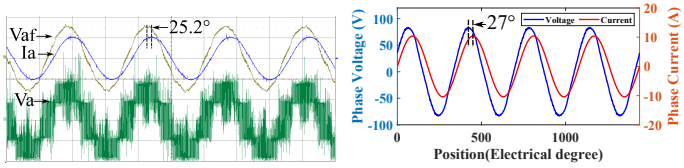

(a) (b)

Fig. 19. A phase voltage and current at 500 r/min (a) Hardware (5 ms/div, 10 A/div and 50 V/div) (b) Simulation

TABLE IV
EXPERIMENTAL RESULTS V/S FEA FOR THE OPTIMAL DESIGN

Situation	Speed (r/min)	Phase current amplitude (A)	Torque (Nm)	TMV (Nm/L)	PF	η (%)
Experiment	500	10.4	17.8	22.5	0.90	86
JMAG (60°C)	500	10.4	18.9	23.8	0.89	87
Proposed analytical	500	10.4	19.45	24.5	0.89	/
Conventional	500	10.4	32.18	40.54	0.96	/

These results indicate that the prototype has achieved the goals of both high torque density and power factor in excellent agreement with the transient FEA simulation (error $< 6\%$) and proposed analytical method (error $< 9\%$).

VI. CONCLUSION

Slot opening and magnet thickness are key geometric parameters for vernier machines and thereby appropriate selection of slot opening and magnet thickness provides a solution for high performance SPMVMs. This paper advances the modeling technique significantly by deriving the air gap permeability function in both radial and tangential directions for leakage flux analysis and proposing a generalized analytical approach for slot opening effect on SPMVMs, which can be utilized to calculate the flux linkage accurately and separate the contribution of each working harmonic. Such modeling improvement indicates the slot opening effect on the high order (equal to rotor pole pair number) flux density is able to significantly decline the flux linkage, thus reducing its contribution to the torque metrics.

This modeling theory is applied to the torque and power factor analysis of SPMVMs. Slot openings and magnetic thickness are evaluated for a high torque density and power

factor design. The FEA approach is conducted to validate the analytical model. It is shown the two methods come in close agreement. Finally, experimental results via a prototype are presented to verify the validity of the analytical model.

REFERENCES

[1] C. Ayers, "Evaluation of 2004 toyota prius hybrid electric drive system interim report," Oak Ridge National Lab.(ORNL), Oak Ridge, TN (United States), Tech. Rep., 2004.

[2] K. Reis and A. Binder, "Comparison of direct drive and high speed drive concepts for the use in wheel-hub-drives," in *8th IET International Conference on Power Electronics, Machines and Drives (PEMD 2016)*, pp. 1–6. IET, 2016.

[3] A. Toba and T. A. Lipo, "Generic torque-maximizing design methodology of surface permanent-magnet vernier machine," *IEEE Trans. Ind. Appl.*, vol. 36, no. 6, pp. 1539–1546, Nov./Dec. 2000.

[4] C. Lee, "Vernier motor and its design," *IEEE Trans. Power App. Syst.*, vol. 82, no. 66, pp. 343–349, 1963.

[5] A. Ishizaki, T. Tanaka, K. Takasaki, and S. Nishikata, "Theory and optimum design of pm vernier motor," in *1995 Seventh International Conference on Electrical Machines and Drives (Conf. Publ. No. 412)*, pp. 208–212. IET, 1995.

[6] X. Zhao, S. Niu, X. Zhang, and W. Fu, "A new relieving-dc-saturation hybrid excitation vernier machine for hev starter generator application," *IEEE Trans. Ind. Electron*, vol. 67, no. 8, pp. 6342–6353, Aug. 2020.

[7] H. Li, Z. Zhu, and Y. Liu, "Optimal number of flux modulation pole in vernier permanent magnet synchronous machines," *IEEE Trans. Ind. Appl.*, vol. 55, no. 6, pp. 5747–5757, Nov./Dec. 2019.

[8] X. Zhao and S. Niu, "Design of a novel parallel-hybrid-excited vernier reluctance machine with improved utilization of redundant winding harmonics," *IEEE Trans. Ind. Electron*, vol. 65, no. 11, pp. 9056–9067, Nov. 2018.

[9] L. Xu, G. Liu, W. Zhao, X. Yang, and R. Cheng, "Hybrid stator design of fault-tolerant permanent-magnet vernier machines for direct-drive applications," *IEEE Trans. Ind. Electron*, vol. 64, no. 1, pp. 179–190, Jan. 2017.

[10] Y. Liu, H. Li, and Z. Zhu, "A high-power factor vernier machine with coil pitch of two slot pitches," *IEEE Trans. Magn.*, vol. 54, no. 11, pp. 1–5, Nov. 2018.

[11] D. Li, R. Qu, and T. A. Lipo, "High-power-factor vernier permanent-magnet machines," *IEEE Trans. Ind. Appl.*, vol. 50, no. 6, pp. 3664–3674, Nov./Dec. 2014.

[12] D. Li, R. Qu, J. Li, L. Xiao, L. Wu, and W. Xu, "Analysis of torque capability and quality in vernier permanent-magnet machines," *IEEE Trans. Ind. Appl.*, vol. 52, no. 1, pp. 125–135, Jan./Feb. 2016.

[13] B. Kim, "Design method of a direct-drive permanent magnet vernier generator for a wind turbine system," *IEEE Trans. Ind. Appl.*, vol. 55, no. 5, pp. 4665–4675, Sep./Oct. 2019.

[14] B. Kim and T. A. Lipo, "Operation and design principles of a pm vernier motor," *IEEE Trans. Ind. Appl.*, vol. 50, no. 6, pp. 3656–3663, Nov./Dec. 2014.

[15] Z. Zhu and D. Howe, "Instantaneous magnetic field distribution in brushless permanent magnet dc motors. iii. effect of stator slotting," *IEEE Trans. Magn.*, vol. 29, no. 1, pp. 143–151, Jan. 1993.

[16] D. K. Padinharu, G. Li, Z. Zhu, M. Foster, D. Stone, A. Griffo, R. Clark, and A. Thomas, "Scaling effect on electromagnetic performance of surface-mounted permanent-magnet vernier machine," *IEEE Trans. Magn.*, vol. 56, no. 5, pp. 1–15, May. 2020.

[17] D. K. Padinharu, G. Li, Z. Zhu, R. Clark, Z. Azar, and A. Thomas, "Investigation of scaling effect on power factor of permanent magnet vernier machines for wind power application," *IET Electr. Power Appl*, vol. 14, no. 11, pp. 2136–2145, 2020.

[18] Z. Zhu, D. Howe, E. Bolte, and B. Ackermann, "Instantaneous magnetic field distribution in brushless permanent magnet dc motors. i. open-circuit field," *IEEE Trans. Magn.*, vol. 29, no. 1, pp. 124–135, Jan. 1993.

[19] T. A. Lipo, *Introduction to AC machine design*. John Wiley & Sons, 2017.

[20] L. Wu, R. Qu, D. Li, and Y. Gao, "Influence of pole ratio and winding pole numbers on performance and optimal design parameters of surface permanent-magnet vernier machines," *IEEE Trans. Ind. Appl.*, vol. 51, no. 5, pp. 3707–3715, Sep./Oct. 2015.

[21] B. Kim and T. A. Lipo, "Analysis of a pm vernier motor with spoke structure," *IEEE Trans. Ind. Appl.*, vol. 52, no. 1, pp. 217–225, 2015.